Electronic materials



Phase and stoichiometry control in superconducting FeSe layers on SrTiO₃

Maria Hilse^{1,2,*}, Forrest Brown¹, Joseph Roth¹, Simon Munyan¹, and Roman Engel-Herbert^{1,3}

Received: 7 November 2023 Accepted: 3 January 2024 Published online: 1 February 2024

© The Author(s), under exclusive licence to Springer Science+Business Media, LLC, part of Springer Nature, 2024

ABSTRACT

Phase and stoichiometry control are crucial to employ the superconducting properties of FeSe thin films, and with it the previously reported interfacial boost in superconductivity promoted by the SrTiO₃ surface. This work investigates how growth parameters influence the phase and chemical composition in FeSe layers on SrTiO₃(001) substrates by molecular beam epitaxy. In the first part, the influence of substrate surface preparation on the stabilization of the respective FeSe phase and film morphology is evaluated by atomic force microscopy (AFM), reflection high energy-electron diffraction (RHEED), and X-ray diffraction (XRD). Continuous, phase-pure β-FeSe layers were observed on non-ideally prepared substrates only at high growth temperatures, whereas optimized surface preparation yielded similar results at much reduced temperatures. Although RHEED indicated atomically smooth film topography, AFM revealed pronounced island growth. In the second part, the stoichiometry of phase-pure β -FeSe films grown under different growth conditions is evaluated by XRD and structural calculations. Supporting transport measurements identified a narrow growth window to satisfy the stoichiometric requirement for superconducting β -FeSe thin films.

Introduction

In 2008, bulk FeSe was reported to be a superconductor with a $T_{\rm c}$ of 9 K at ambient pressures [1]. Further studies achieved a heightened critical temperature of 37 K at a pressure of 8.9 GPa [2]. The most intriguing aspect of FeSe, the structurally simplest of all Fe-based superconductors, is the observed interfacial superconductivity in ultra-thin films grown on SrTiO₃. Critical temperatures ranging from 109 K [3] to 65 K [4–6] were

reported for a single layer of FeSe grown epitaxially on $SrTiO_3(001)$. This significant rise in T_c for the FeSe/ $SrTiO_3$ heterostructure has attracted the attention of the research community to elucidate its superconducting mechanism [7, 8]. A prerequisite to facilitate this investigation is a reliable epitaxial synthesis process that creates superconducting FeSe layers with macroscopic lateral dimensions and precisely tuneable thickness.

Handling Editor: David Cann.

Address correspondence to E-mail: mxh752@psu.edu



¹ Department of Materials Science and Engineering, The Pennsylvania State University, University Park, PA 16802, USA

² Materials Research Institute, The Pennsylvania State University, University Park, PA 16802, USA

³ Paul-Drude Institut für Festkörperelektronik, Leibniz-Institut im Forschungsverbund Berlin e.v., 10117 Berlin, Germany

Molecular beam epitaxy (MBE) growth of superconducting FeSe was reported to have a wide growth window in which the Fe to Se flux ratio can be 1:10 or as high as 1:20. The growth is self-regulating since the sticking coefficient of pure Se is zero in the growth temperature window for FeSe, leaving Fe as the ratedetermining species [9–11]. However, bulk superconducting FeSe only occurs in a narrow stoichiometry range of β -Fe_{1.01}Se to β -Fe_{1.025}Se. The phase diagram presents several non-superconducting phases close to a 1:1 Fe:Se ratio, including tetragonal β-Fe_xSe with x > 1.025 and x < 1.010, hexagonal γ -Fe₇Se₈, hexagonal α -FeSe, and elemental Fe [12]. In addition, a structural transition from tetragonal to orthorhombic is observed at 90 K for the superconducting β -Fe_{1.01}Se, but not the non-superconducting β -Fe_{1.03}Se [13].

β-FeSe has a simple PbO prototype crystal structure with P4/nmm symmetry, space group 129, much simpler in comparison with the superconducting cuprates and other superconducting iron-based materials. This relatively simple structure raises interest in understanding the specific mechanism giving rise to superconductivity in FeSe, which could be subsequently used to design other thin films of similar superconducting materials on various substrates besides SrTiO₃. In comparison with (001)-oriented SrTiO₃ [cubic perovskite crystal structure of Pm3m space group with a lattice parameter of a = 3.91 Å [14], tetragonal (001)-oriented bulk β-FeSe has a smaller inplane lattice parameter of a = 3.77 Å [15] resulting in an approximately 3 % lattice mismatch between FeSe and SrTiO₃. It was shown that the initial preparation of the SrTiO₃ surface plays a significant role in the resulting superconducting properties arising from the FeSe/SrTiO₃ interface [7]. The common understanding of the field is that only TiO₂-terminated SrTiO₃ surface terraces lead to an increase in T_C [7]. Much effort has since been undertaken to prepare solely TiO₂-terminated SrTiO₃, to the point that SrTiO₃ substrates with atomic step morphology claiming TiO₂ surface termination are now commercially available [16]. The preparation of specifically terminated SrTiO₃ substrates is not trivial [17] and requires atomic steps of $(1 \times n)$ unit cell (UC) step height (with *n* being a natural number) across the macroscopic substrate scale, which was shown to be successful only after applying elaborate chemical and thermal treatments or by growing SrTiO₃ buffer layers using oxide MBE with a shuttered growth approach [18–21]. In addition, only scanning tunneling microscopy (STM) and friction force microscopy (FFM) have been identified to reliably probe the substrate surface atomic arrangement, and among the two, only FFM can be used to study surface termination over a macroscopic scale [22–25].

Besides the synthesis, the characterization of FeSe thin films is challenging as well, which is due to the material's extreme air sensitivity that requires characterization in ultra-high vacuum (UHV), or the deposition of a protective cap to prevent the oxidation of FeSe. Typically, tellurium, selenium, or FeTe are used as thin film caps for FeSe [7]. This holds problems as interdiffusion of the chalcogen species at the interface could potentially form FeSe_{1-x}Te_x, and the oxidation of the FeTe cap will eventually lead to FeTe_{1-x}O_x formation. Both ternary compounds are reported superconductors with similar T_C to FeSe, which complicates characterization [26–34].

Studying interfacial superconductivity therefore requires reliable and successful growth of superconducting β -FeSe layers on SrTiO₃. The following four tasks must be accomplished to meet this requirement:

- I. Ultra-clean SrTiO₃ surface preparation with an atomic step structure morphology and defined surface termination over the macroscopic scale.
- II. Preparation of tetragonal superconducting FeSe layers in the stoichiometric composition from β -Fe_{1.01}Se to β -Fe_{1.025}Se.
- III. Precise tuning of the FeSe layer thickness down to the UC limit with uniform sample coverage over macroscopic lateral dimensions.
- IV. Growth of a non-superconducting, inert and preferably insulating capping layer that efficiently screens the FeSe layers from oxidation in air.

In the presented work, we report on requirements (I) and (II) in MBE growth of FeSe. The influence of substrate surface preparation on FeSe phase stabilization and film morphology as well as the capability of *in-situ* morphological and structural monitoring by reflection high-energy electron diffraction (RHEED) is presented in the first part of this work. In the second part, we show that superconducting FeSe thin films, like their bulk derivatives, exist in a stoichiometric narrow growth window. Through our study, XRD is presented as a powerful, straight-forward, fast, and affordable alternative to slow, expensive, localized, and elaborate scanning microscopy techniques for evaluating the stoichiometric composition of the



films with reliable implications on the superconducting properties. Despite extensive efforts to synthesize β -FeSe layers of different thicknesses on SrTiO $_3$ by MBE, we find that the relationship between substrate preparation and phase formation and the study of film morphology and stoichiometry are understudied and remain unanswered [35–37]. Our work thus provides valuable knowledge advantageous to the field of β -FeSe synthesis by MBE.

Methods

Undoped, single-crystal $SrTiO_3(001)$ substrates with ± 0.5 ° non-intentional miscut fabricated in Japan from MTI Corporation were used for this study. After the surface preparation step described in more detail later in Sect. "Results and discussion", substrates were immediately loaded into the load lock and annealed in UHV to 200 °C for 30 min to desorb water films from the substrates.

FeSe and FeTe depositions were carried out in an R450 MBE reactor from DCA Instruments, equipped with individual Knudsen effusion cells that evaporated ultra-pure Fe, Se, and Te charges. Prior to the film depositions Fe, Se, or Te fluxes were calibrated using a model Eon-heated quartz crystal microbalance (QCM) device from Colnatec inserted at the sample position. Tooling factors for flux calibration were found from physical film thickness measurements by XRD. Typical fluxes for Fe were in the order of 3.8×10^{13} cm⁻² s⁻¹, or an FeSe growth rate of 0.17 Å/s. Se and Te fluxes of the order of 2.5-5.5 or higher were supplied to account for the high desorption rate of the chalcogen species and ensure proper FeSe/FeTe phase formation. Film deposition was monitored in-situ by a RHEED system equipped with an electron gun from STAIB Instruments operated at 15 kV and a kSA 400 imaging and processing camera and software package. The background pressure in the MBE reactor was kept at or below 3×10^{-9} Torr during deposition.

Characterization of the film surface morphology was performed ex-situ with a Dimension Icon Bruker atomic force microscope (AFM) operated in PeakForce Tapping mode.

Ex-situ structural characterization was carried out using a four-circle diffractometer (Panalytical X'Pert3) equipped with a PIXcel 3D detector. The XRD setup was operated in high-resolution configuration using Cu $K_{\alpha 1}$ radiation.

Resistivity measurements were taken ex-situ to obtain sheet resistance as a function of temperature. Samples were adhered to a four-probe resistivity puck (Quantum Design Inc.) using a thin coat of GE varnish. Pure indium dots were pressed onto the sample corners according to the van der Pauw geometry. Gold wires were used to connect the indium contacts on the sample to the contacts on the puck. The resistance between each pair of contacts was measured with a multimeter at room temperature to ensure that the contact resistances were similar. Using a Physical Property Measurement System (Quantum Design Inc.), the vertical and horizontal in-plane resistances were measured continually during cooling and heating between (300–2) K at a rate of 8 K/min. The current limit, power limit, and voltage limit through the samples were kept at 1 mA, 1 mW, and 95 mV, respectively. The sheet resistance was then calculated as a function of temperature assuming an isotropic sample.

Results and discussion

Controlling FeSe phase formation and film morphology

AFM was carried out before growth on differently prepared SrTiO₃ samples to investigate the surface morphology of as-received substrates and the effect of different surface treatments on the substrate configuration. The results are shown in Fig. 1. All samples were cleaned by subsequent sequences of 3-min ultrasonic (US) baths in acetone, isopropanol, and DI water after each furnace anneal presented in Fig. 1. The asreceived sample in Fig. 1a displays the most random morphology marked by irregular islands covered by nanoscale spheres. A furnace annealing step to 900 °C for 60 min in air, anneal b in Fig. 1b shows onset of atomic step formation; wide terraces in the order of 400 nm with rough step edges can be seen. Annealing as-received SrTiO₃ substrates in air for 60 min at 1000 °C, i.e., anneal c in Fig. 1c clearly results in surface terrace formation with smooth but sawtoothlike edges that frequently exhibit a double sawtooth feature. The observed step heights after anneal c are 1 UC high for the single and ½ UC high for the double sawtooth step edge features of SrTiO₃ as extracted from AFM line profiles. Thus, anneal c results in a mixed SrO and TiO₂-terminated surface due to the ½-UC steps. A prolonged anneal at 1000 °C in air for



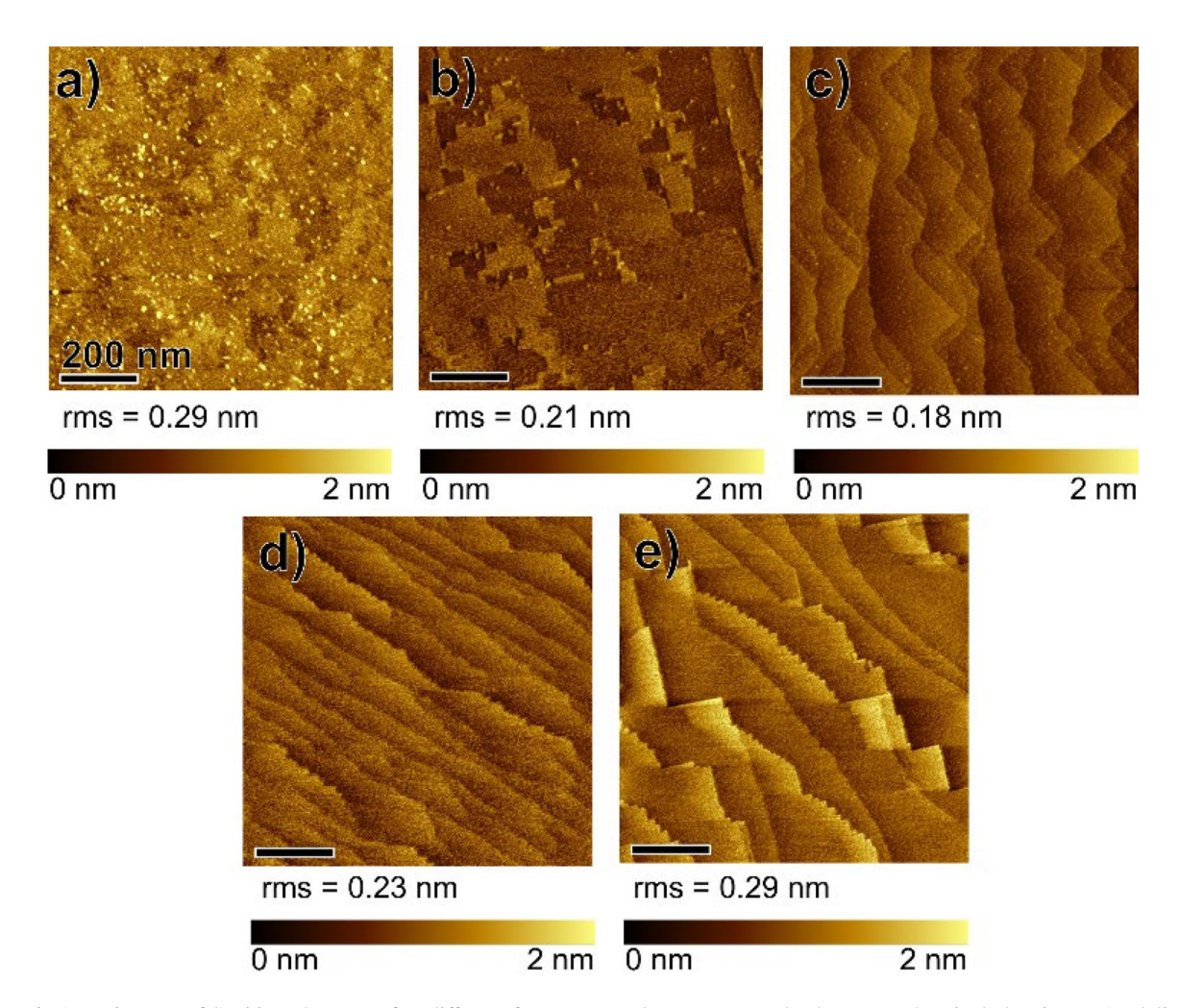


Figure 1 AFM images of SrTiO₃ substrates after different furnace anneal treatments and subsequent chemical cleaning. **a** As-delivered, **b** anneal to 900 °C for 1 h in air, **c** anneal to 1000 °C for 1 h in air, **d** anneal to 1000 °C for 1.5 h in air, **e** anneal to 1000 °C for 2 h in air.

90 min, i.e., anneal d in Fig. 1d leads to the formation of almost perfect 1 UC atomic steps with smooth edges and terrace widths of about 50 nm. Anneal e in Fig. 1e, 120 min at 1000 °C in air, however, does not improve the surface morphology anymore. Although the terrace width increases, the average step height distribution widens and spans from (½–1½) UC SrTiO $_3$ steps, the formerly smooth edges become rough and show pronounced sawtooth features.

Based on the AFM investigation in Fig. 1, anneals c and d were chosen as templates for FeSe growth due to the low root mean square (rms) surface roughness values of 0.18 nm for anneal c and 0.23 nm for anneal d as well as the defined atomic step terrace morphology with step heights in the ($\frac{1}{2}$ -1) UC range.

RHEED and XRD data observed for FeSe growth on SrTiO₃ substrates treated by anneal c are shown in

Fig. 2. The first column shows RHEED images with the top row displaying RHEED of the so-prepared SrTiO₃ substrate, and on the right are the obtained out-ofplane XRD 2Θ - ω -scans after growth. FeSe growth was carried out using an Fe flux of $(3.7–3.8) \times 10^{13}$ cm⁻² s⁻¹ and a Se:Fe flux ratio of 5.5 with varying substrate temperatures from 100 to 500 °C and fixed film thickness of 11 nm, which equals about 20 UC of β-FeSe. The cleanliness and high quality of the surface preparation following anneal c is confirmed by the observation of bright RHEED patterns with a two-fold in-plane symmetry as expected for SrTiO₃ with clearly developed Kikuchi lines. After growth at 100 °C, faint RHEED streaks superimposed by Laure rings and hazy background indicate a low degree of crystal ordering in the FeSe film. XRD shows first- and second-order diffraction peaks of (001)-oriented β -FeSe with an



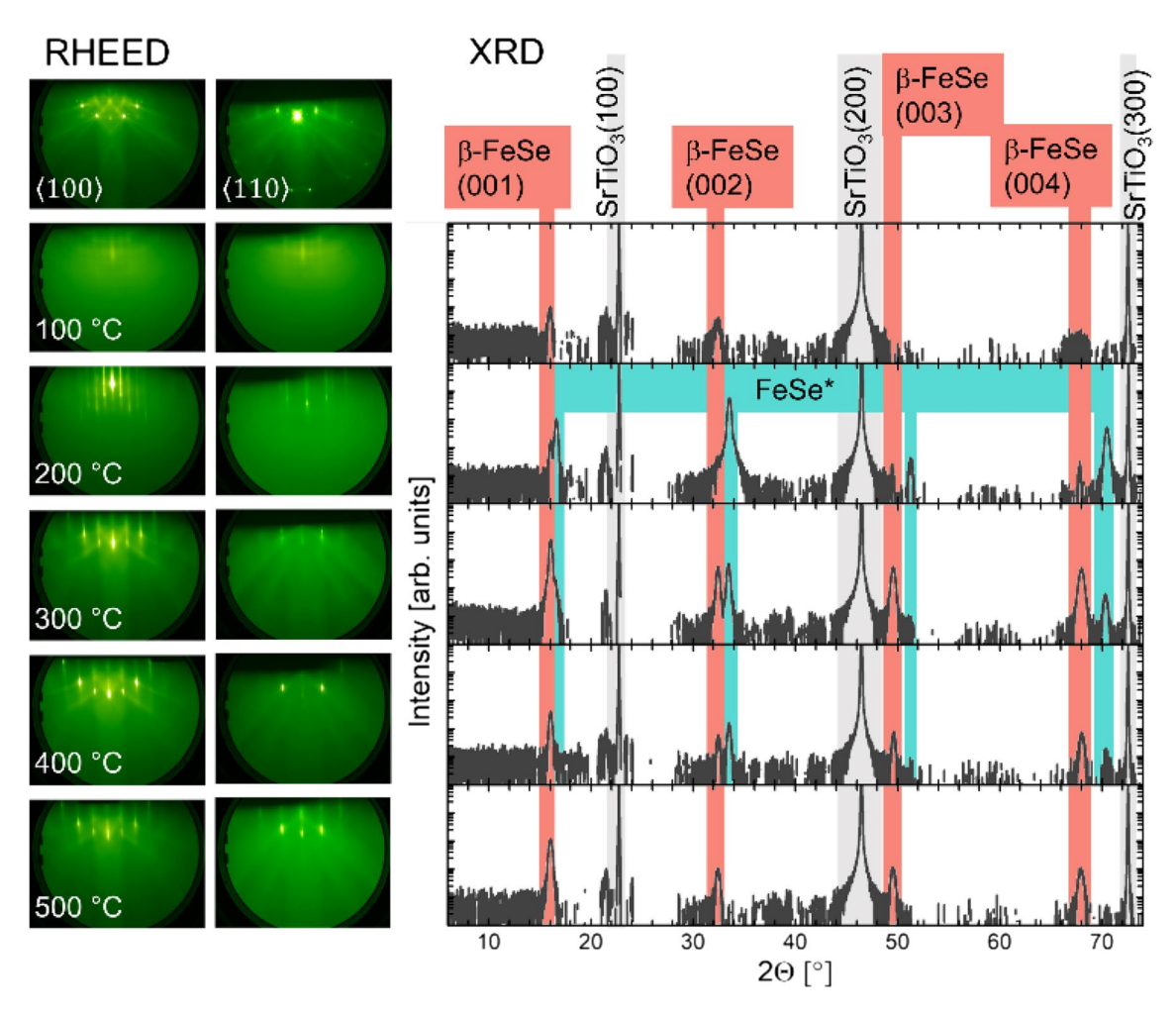


Figure 2 RHEED of $SrTiO_3$ prepared by anneal c top row and after 20 UC FeSe growth at different temperatures. XRD 2Θ-ω-scans obtained from the films on the left denoting the $SrTiO_3$, β-FeSe, and FeSe* peaks by gray, orange, and blue banners, respectively.

out-of-plane lattice constant of c = 5.52 Å in agreement with the literature [12, 13, 38-42]. Growth at 200 °C yields predominantly RHEED streaks, and the crystallinity in the film is thus improved. XRD however reveals the formation of two phases with the second phase labeled FeSe*, which dominates over β-FeSe by XRD peak intensities. The observed FeSe* phase exhibits an out-of-plane lattice parameter of 5.34 Å as extracted from XRD, which can be attributed to the metastable cubic form of FeSe, with a reported lattice parameter of $a = (5.37 \pm 0.05)$ A [43]. The symmetry in the in-plane RHEED diffraction patterns also agrees with a cubic phase formation with a lattice parameter close to the observed 5.34 Å. On the other hand, due to the large variety in reported FeSe phases and corresponding lattice parameters, the presented RHEED and XRD data cannot rule out the possibility that the FeSe* diffractions correspond to the hexagonal FeSe phase [42, 44]. A growth temperature of 300 °C gives highly crystalline diffraction streaks in RHEED corresponding to the symmetry of β-FeSe with no signs of second phase formation. Kikuchi lines are well developed, indicating the significantly increased degree of crystallinity in the film. XRD proves predominantly β-FeSe phase formation by dominating β-FeSe-related peak intensities and a high degree of crystallinity as diffraction peaks from first to fourth order of β-FeSe are visible. However, the second phase is still present in XRD. Temperatures of 400-500 °C appear equally good in RHEED as the 300 °C sample. XRD shows a slight overall intensity decrease at 400 and 500 °C compared to 300 °C for the β-FeSe phase. The formation of the second phase however is finally suppressed at 500 °C.

To realize phase-pure and highly crystalline β -FeSe films on SrTiO₃ substrates prepared with anneal



c thus requires substrate temperatures of 500 °C, which agrees with earlier work that observed a transition of the cubic FeSe phase into the hexagonal and subsequently the tetragonal β -FeSe phase upon annealing to 200 and 300 °C, respectively [43].

RHEED and XRD obtained from FeSe growth on SrTiO₃ prepared by recipe d in Fig. 1d for different Se to Fe flux ratios of 2.5, 5.0, and 7.0 at a growth temperature of 300 °C are shown in Fig. 3. For those three samples, the Fe flux supplied was kept constant at 3.8×10^{13} cm⁻² s⁻¹, and the total deposited film thickness was 20 UC. Although the substrate morphology is strikingly different between the two substrate preparation recipes c and d as seen in Fig. 1, RHEED images obtained from the substrate prepared by anneal d, i.e., top row of Fig. 3 and the respective ones resulting from anneal c, i.e., top row of Fig. 2, are close to identical and agree well with RHEED published for clean, stoichiometric SrTiO₃ films with a (2 × 1) reconstruction [17, 45, 46]. As RHEED is reported to be sensitive to the surface termination of SrTiO₃ on a macroscopic scale with a (1×1) unreconstructed pattern for SrO and a $c(4 \times 4)$ reconstruction for TiO_2 termination, [17] we can conclude that both surface preparation recipes c and d yield mixed-terminated SrTiO₃. FeSe growth at 300 °C on SrTiO₃ prepared by recipe d results in single-crystal diffraction streaks with a symmetry corresponding to β -FeSe for all investigated Se to Fe flux ratios. XRD reveals formation of solely β -FeSe in all samples shown in Fig. 3. The overall diffraction peak intensity however decreases with decreasing Se to Fe flux ratio.

While substrate preparation recipe c leads to mixed β/*-FeSe phases at 300 °C and the second phase formation could only be suppressed at a temperature of 500 °C, recipe d yields single β-FeSe phase formation even at 300 °C. Substrate preparation thus plays a crucial role for FeSe phase nucleation. Given that both recipes c and d produce mixed SrO/TiO₂-terminated SrTiO₃ surfaces, our results imply that a surface morphology of atomic step terraces with 1 UC height and smooth edges facilitate growth of solely β -FeSe phase. On the other hand, the higher-temperature furnace anneal d might have been more effective in removing surface absorbates, which could serve as unintentional nucleation centers, thus leading to a cleaner starting growth template promoting epitaxy and β-FeSe formation. While more in-depth studies of the chemical composition of the starting SrTiO₃ surface are necessary to elucidate the mechanism of FeSe phase formation on SrTiO₃, this work outlines the importance of substrate preparation for FeSe MBE growth.

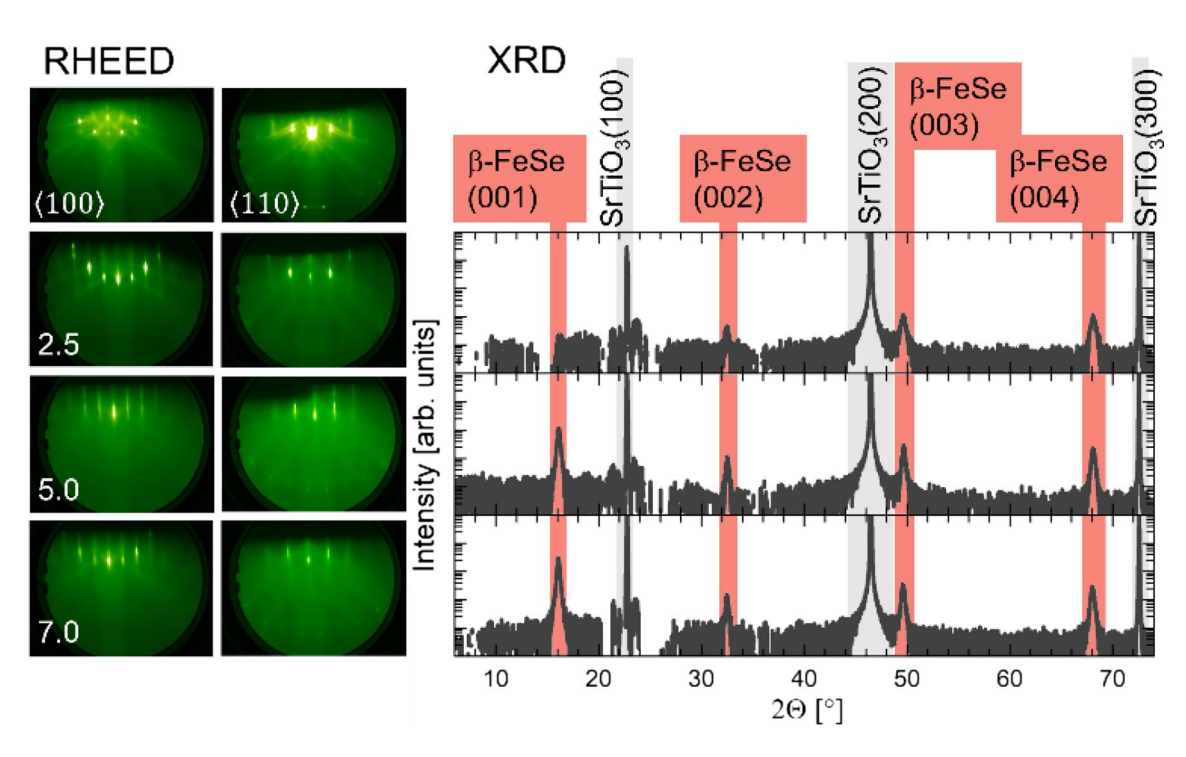


Figure 3 RHEED of SrTiO₃ prepared by anneal d top row and after 20 UC FeSe growth at 300 °C with Se/Fe flux ratios of 2.5, 5.0, and 7.0. XRD 2Θ - ω -scans obtained from the films on the left.



Once the SrTiO₃ surface preparation was optimized to produce the desired β -FeSe phase, we studied the surface morphology of capped films, i.e., FeTe/FeSe heterostructures. Figure 4 presents RHEED, XRD, and AFM images of two samples with 20- and 50-UC thick FeSe capped with 25- and 50-UC thick FeTe on SrTiO₃ substrates, respectively. The FeSe layer was grown at 300 °C and a flux ratio of 4.5, whereas the FeTe cap was grown at 250 °C, and a 4.5-times Te oversupply. Both samples look comparably good in RHEED before and after FeSe and FeTe growth with intense diffraction streaks indicating single-crystal FeSe/FeTe layer formation with smooth interfaces and surfaces. XRD similarly shows single crystal layers of β -FeSe and FeTe with a high degree of crystallinity as diffraction peaks up to the fourth order are visible for both film and capping layers. However, AFM investigation reveals pronounced island formation and rough surface topography reaching rms values of 9 nm. The average height of the observed islands is 35 and 60 nm, respectively, from the height scale of the AFM images. Those values are equally large or larger than the total nominally deposited heterostructure thickness, which amounts to 28 and 60 nm, respectively, in the two samples. Therefore, one can assume that the dark spots, i.e., lowest points observed in the AFM morphology correspond to the bare SrTiO₃ substrate. Although the islands possess large footprints up to lateral dimensions of 500-800 nm, no continuous film forms on the substrate but large, rectangular-shaped isolated islands. Even for the 50-UC FeSe sample, the islands are not fully coalesced over the entire sample area.

Such pronounced island formation behavior prohibits studying the transport properties on the presented FeSe/FeTe heterostructures as films become electrically insulating with decreased film or island coalescence. While evident in AFM, signatures of the observed 3D islands are notably absent in RHEED. This is likely caused by the distinct mesa shape of the islands, where the RHEED beam almost exclusively probes the ultrasmooth island top surfaces only. Through the comparably large lateral dimensions of the islands, and their relatively small height deviations between individual islands, they appear as a smooth and homogeneous film in RHEED. Besides substrate preparation, homogeneous wetting of the SrTiO₃ substrate by FeSe thus turned out to be non-trivial. Coalesced layers with smooth enough morphology that enable transport measurements were only realized on freshly prepared, ultra-clean SrTiO₃ substrates. *In-situ* RHEED analysis however proved itself unsuitable to predict the FeSe growth quality.

Stoichiometry control in β -FeSe by XRD

To study the stoichiometric composition of β-FeSe films, XRD scans of six samples, labeled samples A through F, are compared in Fig. 5. This time, samples were grown under different growth conditions on SrTiO $_3$ substrates prepared by anneal d. All samples consist of an 18-UC-thick FeSe layer capped at 250 °C with an 18-UC-thick layer of FeTe. An overview of the FeSe growth conditions is given in Table 1.

All samples show diffractions corresponding to β -FeSe and FeTe up to the fourth order in XRD. The peak intensities however show a consistent decrease from sample A to F. This drop was captured by extracting the peak intensity ratios of (001)/(002) for the β -FeSe-related diffractions (001) and (002) as noted in the fourth column in Table 1. Total XRD peak intensities were extracted experimentally by first removing the background intensity of the 2Θ - ω -scan before fitting the FeSe-related (001) and (002) diffraction peaks. The so found integrated respective peak intensity was used to calculate the (001)/(002) peak intensity ratio. Overall, we see a drop from 65 in intensity ratio for sample A down to 7 for sample F.

As changes in stoichiometry of any crystal translate directly into changes of the XRD structure factor, structural calculations were performed for β -FeSe to extract the stoichiometry of the presented films. Assuming the standard room temperature crystal structure (P4/nmm) for β -FeSe with a = 3.77 Å and c = 5.48 Å, the peak intensity ratios were then calculated as a function of Se occupancy. This was implemented by first calculating the structure factor, F_{HKL} , given by:

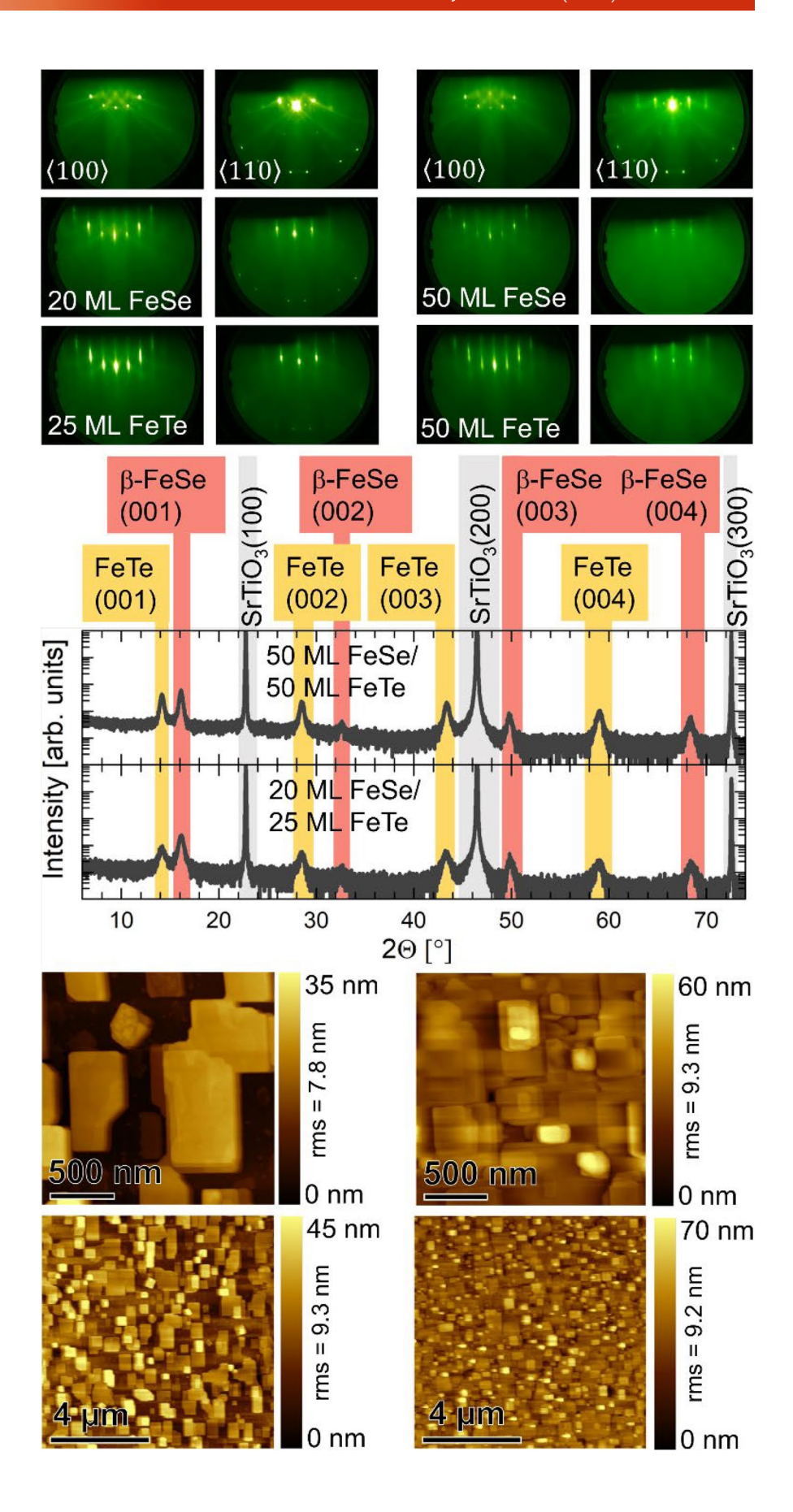
$$F_{HKL} = f_{Fe} \sum_{n=1}^{2} e^{2\pi i (Hu_n + Kv_n + Lw_n)} + f_{Se} \sum_{m=1}^{2} e^{2\pi i (Hu_m + Kv_m + Lw_m)}$$

where f_{Fe} and f_{Se} are the atomic form factors of iron and selenium [47]; H, K, and L are the Miller indices for a given Bragg peak; u, v, and w denote the atomic positions for FeSe given by: Fe = (0,0,0), (0,0,1), Se = (0, 0.5, 0.26), (0.5, 0, 0.74). The intensity of each Bragg peak was then calculated from:

$$I = I_0 L_{\rm PA} |F_{HKL}|^2$$



Figure 4 RHEED, XRD, and AFM images of β-FeSe layers with 20 and 50 UC thickness capped with 25 and 50 UC FeTe on SrTiO $_3$ (001) substrates grown at 300 °C, respectively. The FeTerelated diffraction peaks are indicated by yellow banners.





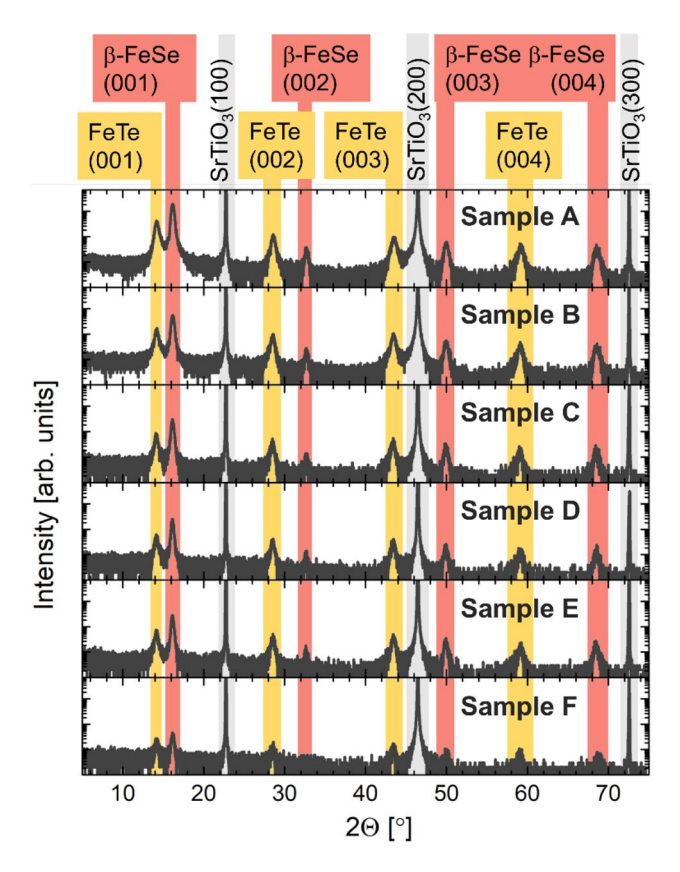


Figure 5 XRD 2Θ-ω-scans obtained from samples A through F exhibiting decreasing XRD peak intensity ratios of FeSe(001)/ FeSe(002)-related diffractions from top to bottom.

Table 1 Substrate temperature $[T_{\rm sub}$ (FeSe)] and Se to Fe flux ratio during FeSe growth, diffraction peak intensity ratios (001)/ (002) as extracted from XRD scans presented in Fig. 5, and calculated Se contents of samples A through F

Sample	T _{sub} (FeSe) (°C)	Se:Fe flux ratio	(001)/(002)	Se content
A	500	4.5	65±5	0.95 ± 0.01
В	500	4.6	30 ± 3	1.04 ± 0.01
C	400	4.0	26 ± 3	1.06 ± 0.02
D	300	3.7	30 ± 3	1.04 ± 0.01
E	350	3.7	24 ± 6	1.07 ± 0.03
F	500	10.5	7 ± 7	≥1.20

where $L_{\rm PA}$ is the Lorentz polarization and absorption correction.

The intensity ratios of first and second orders over Se content in the β -FeSe phase are shown in Fig. 6 by the dark blue circles connected by a line. Although

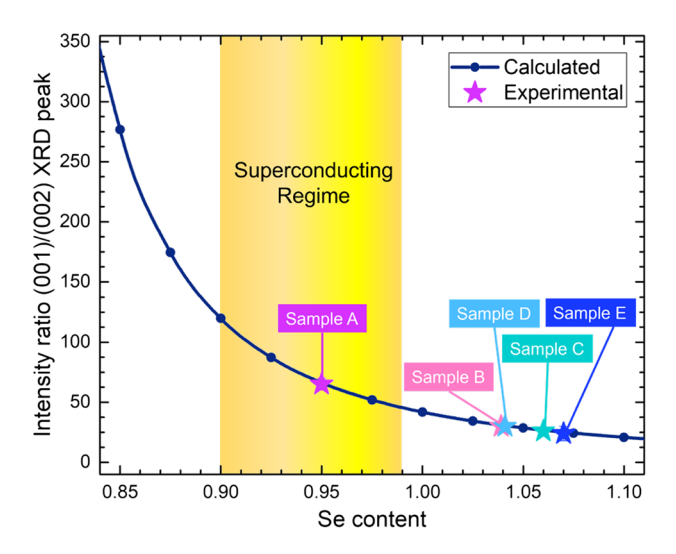


Figure 6 Overlay of the XRD peak intensity ratio FeSe(001)/FeSe(002)-related diffractions versus Se content in the tetragonal FeSe phase found by structural calculations in dark blue circles connected with a line and experimentally obtained values from samples A through F plotted as stars. The published Se content range for superconducting films is highlighted by the yellow area.

the required stoichiometry for observing the superconducting properties in FeSe varies across different reports, the maximum lower and upper published Se content boundaries range from 0.90 to 0.99, respectively [12, 38, 39, 41]. This range is highlighted in Fig. 6 as Se content window required for accessing the superconducting regime in yellow. Differences between the values of individual reports are most likely due to different experimental methods of evaluating the Fe and Se content.

Comparing the experimentally determined diffraction peak ratios given in Table 1 to the structural calculation presented in Fig. 6 allows us to extract the stoichiometry of the films. The amount of Se for samples A through F is given in the last column of Table 1 and overlayed using star symbols in Fig. 6. Only sample A shows a net Se deficiency of about 5 % and thus ranges within the superconducting stoichiometry window. Samples B to F contain more than 50 % Se in the FeSe phase. For sample F, the experimental error bars only allowed for the determination of a lower Se content boundary of 1.20. Structural calculations thus suggest that a diffraction peak intensity ratio (001)/(002) higher than 30 is required in FeSe thin films to observe the superconducting properties.

To test this result, temperature-dependent transport measurements were taken on all samples as presented in Fig. 7. The film sheet resistance was measured over



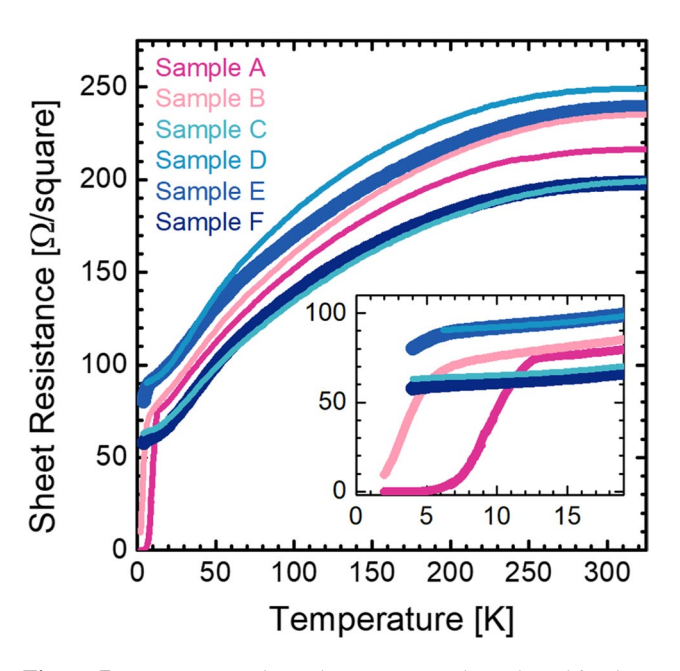


Figure 7 Temperature-dependent transport data plotted in sheet resistance versus temperature obtained for samples A through F. The inset is enlarging the low-temperature behavior.

a range from room temperature down to (2-4) K for samples A through F. The inset in Fig. 7 shows the low-temperature region only for better visibility. Only one of the six samples, sample A with the highest XRD peak intensity ratio of 65, shows the expected superconducting transition temperature of about 9 K typical for β -FeSe. Sample B exhibits the onset of a transition into superconductivity but does not reach the zeroresistance state in the probed temperature window. For samples C to F, no phase transition is apparent in the transport data. Figure 6 furthermore demonstrates that no indication about the superconducting properties can be obtained from the film resistance values at room temperature. These transport measurements thus confirm the conclusions derived from the structural considerations implied by XRD analysis, namely, that only sample A consists of the correct stoichiometry to exhibit superconducting properties. For all other samples, however, growth conditions were at the edge (sample B) and outside of the compositional window for superconductivity in β -FeSe. Although samples B and D present identical stoichiometry, the error margin between the two samples allows for a difference of 2 % in Se/Fe composition between the two samples. This is likely the reason why sample B shows a clear transition toward a superconducting state while sample D does not.

Probing the structure factor of the β -FeSe phase by XRD gives a reliable indication about the superconducting properties of the film. Therefore, XRD can serve as a powerful tool to probe the stoichiometry in the β -FeSe layers, which is typically a much faster and cheaper feedback loop for growth engineering of superconducting β -FeSe than time-consuming temperature-dependent transport measurements.

Conclusions

In summary, this study demonstrated how substrate preparation is essential in stabilizing the β-FeSe phase. Mixed phase films were observed on non-ideally prepared SrTiO₃(001) surfaces under a variety of growth parameters. However, exclusively phase-pure β-FeSe films were realized when growing on optimized SrTiO₃(001) surfaces. The degree to which the growth relies on a specific surface morphology of atomically smooth terrace steps and a sufficiently high degree of cleanliness of the starting SrTiO₃(001) surface remains to be answered. Surprisingly, RHEED was shown to be unreliable for evaluating the FeSe thin film morphology during and after growth. This we attribute to the distinct mesa shape of the observed FeSe and FeTe islands developing under diverse growth parameters. XRD, however, proved to be a powerful, fast, and accessible tool to evaluate the stoichiometric composition of the FeSe thin films and predict the superconducting properties of the synthesized films. According to our study, an XRD (001)/(002) intensity ratio between 38 and 120 will indicate a Se content of 0.99 and 0.90, respectively. In agreement with previous reports, FeSe films with an intensity ratio within this window are highly likely to exhibit superconducting properties.

Acknowledgements

This work was supported by The Pennsylvania State University Two-Dimensional Crystal Consortium—Materials Innovation Platform (2DCC-MIP). 2DCC-MIP is supported by NSF cooperative Agreements No. DMR-1539916 and DMR-2039351.



Author contributions

MH lead conceptualization, investigation, methodology, project administration, validation, visualization, as well as writing-original draft and - review and editing of the work. MH contributed to data curation, formal analysis, and supervision of the presented study. FB contributed to data curation, formal analysis, investigation, methodology, project administration, validation, visualization, and writing-original draft of this manuscript. JR contributed to data curation, formal analysis, validation, writing-original draft, and visualization of this work. SM contributed to data curation, validation, and writing-original draft of the presented work. REH lead funding acquisition, supervision, and provided the resources for carrying out this study. Further REH contributed to conceptualization, investigation, methodology, and project administration of this work. All authors contributed to writing-review and editing of the presented work.

Data availability

All relevant data supporting this work is contained in the manuscript and available publicly at http://data. 2dccmip.org/10.26207/q386-br66 or at ScholarSphere under DOI: 10.26207/q386-br66 (https://doi.org/10.26207/q386-br66).

Declarations

Conflicts of interest Authors declare that there are no conflicts of interest.

Ethical approval Not applicable.

References

[1] Wang MJ, Luo JY, Huang TW, Chang HH, Chen TK, Hsu FC, Wu CT, Wu PM, Chang AM, Wu MK (2009) Crystal orientation and thickness dependence of the superconducting transition temperature of tetragonal FeSe1-x thin films. Phys Rev Lett 103:117002. https://doi.org/10.1103/PhysRevLett.103.117002

- [2] Medvedev S et al (2009) Electronic and magnetic phase diagram of β -Fe1.01Se with superconductivity at 36.7 K under pressure. Nat Mater 8:630–633
- [3] Ge J, Liu ZL, Liu C, Gao C, Qian D, Xue Q, Liu Y, Jia JF (2014) Superconductivity above 100 K in single-layer FeSe films on doped SrTiO3. Nat Mater 14:285–289
- [4] Lee JJ et al (2014) Interfacial mode coupling as the origin of the enhancement of Tc in FeSe films on SrTiO3. Nature 515:245–248
- [5] Tan S et al (2013) Interface-induced superconductivity and strain-dependent spin density waves in FeSe/SrTiO3 thin films. Nat Mater 12:634–640
- [6] He S et al (2013) Phase diagram and electronic indication of high-temperature superconductivity at 65 K in singlelayer FeSe films. Nat Mater 12:605–610
- [7] Huang D, Hoffman JE (2017) Monolayer FeSe on SrTiO3. Annu Rev Condens Matter Phys 8:311–336
- [8] Bozovic I, Ahn C (2014) A new Frontier for superconductivity. Nat Phys 10:892–895
- [9] Song CL, Wang YL, Jiang YP, Li Z, Wang L, He K, Chen X, Ma XC, Xue QK (2011) Molecular-beam epitaxy and robust superconductivity of stoichiometric FeSe crystalline films on bilayer graphene. Phys Rev B 84:020503. https://doi.org/10.1103/PhysRevB.84.020503
- [10] Liu DSH, Hilse M, Engel-Herbert R (2021) Sticking coefficients of selenium and tellurium. J Vac Sci Technol, A 39:023413. https://doi.org/10.1116/6.0000736
- [11] Liu DSH, Hilse M, Engel-Herbert R (2022) Desorption characteristics of selenium and tellurium thin films. J Vac Sci Technol, A 40:053407. https://doi.org/10.1116/6.00020 13
- [12] McQueen TM et al (2009) Extreme sensitivity of superconductivity to stoichiometry in Fe1+dSe. Phys Rev B 79:014522. https://doi.org/10.1103/PhysRevB.79.014522
- [13] McQueen TM, Williams AJ, Stephens PW, Tao J, Zhu Y, Ksenofontov V, Casper F, Felser C, Cava RJ (2009) Tetragonal-to-orthorhombic structural phase transition at 90 K in the superconductor Fe1.01Se. Phys Rev Lett 103:057002. https://doi.org/10.1103/PhysRevLett.103.057002
- [14] Schmidbauer M, Kwasniewski A, Schwarzkopf J (2012) High-precision absolute lattice parameter determination of SrTiO3, DyScO3 and NdGaO3 single crystals. Acta Crystallogr B 68:8–14
- [15] Böhmer AE, Hardy F, Eilers F, Ernst D, Adelmann P, Schweiss P, Wolf T, Meingast C (2013) Lack of coupling between superconductivity and orthorhombic distortion in stoichiometric single-crystalline FeSe. Phys Rev B 87:180505. https://doi.org/10.1103/PhysRevB.87.180505
- [16] MTI Corporation. https://www.mtixtl.com/STEP-SrTiO3-Imported-from-Japan.aspx



- [17] Kajdos AP, Stemmer S (2014) Surface reconstructions in molecular beam epitaxy of SrTiO3. Appl Phys Lett 105:191901. https://doi.org/10.1063/1.4901726
- [18] Kubo T, Nozoye H (2003) Surface structure of SrTiO3(100). Surf Sci 542:177–191
- [19] Castell MR (2002) Scanning tunneling microscopy of reconstructions on the SrTiO3() surface. Surf Sci 505:1–13
- [20] Biswas A, Yang C-H, Ramesh R, Jeong YH (2017) Atomically flat single terminated oxide substrate surfaces. Prog Surf Sci 92:117–141
- [21] Haeni JH, Theis CD, Schlom DG (2000) RHEED intensity oscillations for the stoichiometric growth of SrTiO3 thin films by reactive molecular beam epitaxy. J Electroceram 2/3:385–391
- [22] Koster G, Kropman BL, Rijnders GJHM, Blank DHA, Rogalla H (1998) Quasi-ideal strontium titanate crystal surfaces through formation of strontium hydroxide. Appl Phys Lett 73:2920–2922
- [23] Lin Y, Becerra-Toledo AE, Silly F, Poeppelmeier KR, Castell MR, Marks LD (2011) The (2×2) reconstructions on the SrTiO3 (001) surface: a combined scanning tunneling microscopy and density functional theory study. Surf Sci 605:L51–L55
- [24] Gunnarsson R, Kalabukhov AS, Winkler D (2009) Evaluation of recipes for obtaining single terminated perovskite oxide substrates. Surf Sci 603:151–157
- [25] Connell JG, Isaac BJ, Ekanayake GB, Strachan DR, Seo SSA (2012) Preparation of atomically flat SrTiO 3 surfaces using a deionized-water leaching and thermal annealing procedure. Appl Phys Lett 101:251607. https://doi.org/10.1063/1.4773052
- [26] Cho D, Bastiaans KM, Chatzopoulos D, Gu GD, Allan MP (2019) A strongly inhomogeneous superfluid in an ironbased superconductor. Nature 571:541–545
- [27] Wang Z, Rodriguez JO, Jiao L, Howard S, Graham M, Gu GD, Hughes TL, Morr DK, Madhavan V (2020) Evidence for dispersing 1D Majorana channels in an iron-based superconductor. Science 367:104–108
- [28] Gray MJ et al (2019) Evidence for helical hinge zero modes in an Fe-based superconductor. Nano Lett 19:4890–4896
- [29] Machida T, Sun Y, Pyon S, Takeda S, Kohsaka Y, Hanaguri T, Sasagawa T, Tamegai T (2019) Zero-energy vortex bound state in the superconducting topological surface state of Fe(Se, Te). Nat Mater 18:811–815
- [30] Ma Q, Xu S-Y, Shen H, et al (2019) Observation of the nonlinear Hall effect under time-reversal-symmetric onditions. Nature 565:337–342. https://doi.org/10.1038/ s41586-018-0807-6
- [31] Hu H, Kwon JH, Zheng M, Zhang C, Greene LH, Eckstein JN, Zuo JM (2014) Impact of interstitial oxygen on

- the electronic and magnetic structure in superconducting Fe1+yTe Ox thin films. Phys Rev B Condens Matter Mater Phys 90:180504. https://doi.org/10.1103/PhysRevB.90.180504
- [32] Telesca D, Nie Y, Budnick JI, Wells BO, Sinkovic B (2012) Impact of valence states on the superconductivity of iron telluride and iron selenide films with incorporated oxygen. Phys Rev B Condens Matter Mater Phys 85:214517. https://doi.org/10.1103/PhysRevB.85.214517
- [33] Zheng M (2013) Superconductivity in oxygen doped iron telluride by molecular beam epitaxy. Dissertation, University of Illinois at Urbana-Champaign
- [34] Nie YF, Telesca D, Budnick JI, Sinkovic B, Wells BO (2010) Superconductivity induced in iron telluride films by low-temperature oxygen incorporation. Phys Rev B Condens Matter Mater Phys 82:020508. https://doi.org/ 10.1103/PhysRevB.82.020508
- [35] Venzmer E, Kronenberg A, Maletz J, Jourdan M (2015) Morphology of superconducting FeSe thin films deposited by co-sputtering and MBE. https://doi.org/10.48550/arXiv. 1505.02630
- [36] Huang Y, Ren S (2023) Controlled growth and chemical engineering of FeSe-based superconducting films. Adv Phys Res 2:2200058. https://doi.org/10.1002/apxr.20220 0058
- [37] Zhang Y, Zhang ZM, Nie JH, Zhang W, Fu YS (2023) Atomic construction and spectroscopic characterization of FeSe-derived thin films on SrTiO3 substrates. AAPPS Bull 33:30. https://doi.org/10.1007/s43673-023-00106-2
- [38] Pomjakushina E, Conder K, Pomjakushin V, Bendele M, Khasanov R (2009) Synthesis, crystal structure, and chemical stability of the superconductor FeSe1-x. Phys Rev B Condens Matter Mater Phys 80:024517. https://doi.org/10. 1103/PhysRevB.80.024517
- [39] de Souza M, Haghighirad AA, Tutsch U, Assmus W, Lang M (2010) Synthesis, structural and physical properties of δ'-FeSe1 -x. Eur Phys J B 77:101–107
- [40] Nitsche F, Goltz T, Klauss H-H, Isaeva A, Müller U, Schnelle W, Simon P, Doert T, Ruck M (2012) Room-temperature synthesis, hydrothermal recrystallization, and properties of metastable stoichiometric FeSe. Inorg Chem 51:7370–7376
- [41] Rani S, Varma GD (2013) Effect of Sb and Si doping on the superconducting properties of FeSe0.9. Phys C Supercond 485:137–144
- [42] Okamoto H (1991) The Fese (Ironselenium) system. J Phase Equilib 12:383–389
- [43] Shivastava MM, Srivastava ON (1975) Studies of structural transformations and electrical behaviour of FeSe Films. Thin Solid Films 29:275–284



- [44] The Materials Project (2020) Data retrieved from the Materials Project for FeSe (mp-1090) from databaseversion v2023.11.1. In: Materials Data on FeSe by Materials Project. https://materialsproject.org/materials/mp-1090/
- [45] Jalan B, Cagnon J, Mates TE, Stemmer S (2009) Analysis of carbon in SrTiO3 grown by hybrid molecular beam epitaxy. J Vac Sci Technol, A: Vac, Surf Films 27:1365–1368
- [46] Lapano J, Brahlek M, Zhang L, Roth J, Pogrebnyakov A, Engel-Herbert R (2019) Scaling growth rates for perovskite oxide virtual substrates on silicon. Nat Commun 10:2464. https://doi.org/10.1038/s41467-019-10273-2
- [47] Brown PJ, Fox AG, Maslen EN, O'Keefe MA, Willis BTM (2006) Intensity of diffracted intensities. International

tables for crystallography. International Union of Crystallography, Chester, pp 554–595

Publisher's Note Springer Nature remains neutral with regard to jurisdictional claims in published maps and institutional affiliations.

Springer Nature or its licensor (e.g. a society or other partner) holds exclusive rights to this article under a publishing agreement with the author(s) or other rightsholder(s); author self-archiving of the accepted manuscript version of this article is solely governed by the terms of such publishing agreement and applicable law.

